nature communications

Article

https://doi.org/10.1038/s41467-026-69046-3

Dynamic plastic deformation delocalization in FCC solid solution metals

Received: 16 June 2025

Accepted: 23 January 2026

Published online: 02 February 2026

Check for updates

Dhruv Anjaria[1], Milan Heczko[2], Daegun You[3], Mathieu Calvat[1], Shuchi Sanandiya[1], Maik Rajkowski[4], Aditya Srinivasan Tirunilai[4], Huseyin Sehitoglu[3], Guillaume Laplanche[4] & J. C. Stinville[1]

Metallic materials undergo irreversible deformation under mechanical loading, leading to intense local plastic localization that reduces their mechanical performance. We identify a mechanism of plastic deformation that dynamically promotes the homogenization of plasticity in face-centered cubic solid solution-strengthened metallic alloys. We observe that this mechanism occurs within a narrow range of stacking fault energies and involves competing deformation between nanoscale twinning and slip. This phenomenon is attributed to a new mechanism referred to as dynamic plastic deformation delocalization, which opens a new design space for enhancing the mechanical performance of metallic materials. We demonstrate that the activation of this mechanism has a significant impact on fatigue properties, greatly enhancing fatigue strength when it occurs.

Metallic materials have critical importance since they are used in a vast range of structural applications[1] across a wide range of temperatures due to their excellent monotonic mechanical properties, including yield strength, ultimate tensile strength, ductility, and toughness[2,3]. These properties originate from their atomic structure and engineered microstructure, which provide substantial strengthening and effectively accommodate defects and deformation[4–6].

Their microstructure is often designed to exhibit significant heterogeneity, creating barriers to defect motion, such as dislocations, and promoting beneficial deformation mechanisms[7,8]. Through this design approach, these microstructural barriers provide exceptional strength to the material[7]. However, this microstructure heterogeneity leads to highly localized plasticity at small scales, concentrating deformation within specific regions of the material[9]. Consequently, these regions become highly susceptible to damage under cyclic loading (i.e., fatigue)[10–13].

As increasingly engineered microstructures are designed to exhibit unprecedented monotonic strength, the fatigue efficiency of these materials tends to decrease[9,14,15]. Fatigue efficiency can be described by the fatigue ratio[15], defined as the fatigue strength normalized by the yield or ultimate tensile strength. When examining the fatigue ratio as a function of the yield or ultimate tensile strength for a large set of metallic materials, a significant decrease in the fatigue ratio is observed with increasing strength[9,15]. In many cases, highly engineered materials with high strength can fail by fatigue at stresses as low as 25% of their yield strength, highlighting a notably low fatigue efficiency. High-strength materials, such as superalloys[16,17] and titanium alloys[18], are examples of highly engineered materials that exhibit high strength but low fatigue efficiency. Therefore, fatigue remains a critical design consideration for structural materials.

This trade-off between monotonic strength and fatigue strength arises from the intense localization of plasticity and its irreversibility that occurs in metallic materials[9,10,19,20]. This relationship has been qualitatively demonstrated in metallic materials that deform by slip[9], where statistical measurements of slip localization intensity (*i.e.* plasticity localization induced by slip) have been related to the fatigue ratio. As slip localization intensity increases, the fatigue ratio (*i.e.*, fatigue efficiency) decreases, and vice versa[9]. In face-centered cubic (FCC) and hexagonal close-packed (HCP) materials, reducing the intensity of plasticity localization without compromising monotonic strength is challenging, as high yield strength FCC and HCP materials

[1]Materials Science & Engineering Department, University of Illinois Urbana-Champaign, Urbana, IL, USA. [2]Institute of Physics of Materials, Czech Academy of Sciences, Brno, Czech Republic. [3]Mechanical Science & Engineering Department, University of Illinois Urbana-Champaign, Urbana, IL, USA. [4]Institut für Werkstoffe, Ruhr-Universität Bochum, Bochum, Germany. e-mail: anjaria3@illinois.edu; jcstinv@illinois.edu

consistently exhibit intense plastic localization. This intense plastic localization is significantly pronounced in FCC materials at room temperature, where thermally activated cross-slip is unfavorable. In contrast, when cross-slip is promoted, such as at high temperatures for FCC materials or at room temperature for BCC materials, the intensity of plastic localization decreases significantly, and the fatigue ratio thus improves[21,22].

Massively promoting cross-slip in FCC materials to minimize the intensity of plastic localization is challenging and we are therefore seeking to identify either processing or microstructures that will provide low levels of plastic localization. One potential solution is to delocalize plastic deformation through conceptual mechanisms that lead to homogenized plasticity during deformation. It has been demonstrated as being possible in HCP materials by either identifying microstructures that homogenize plasticity or by activating mechanisms that promote plastic homogenization[23–25]. However, no such mechanism or evidence of this effect on fatigue strength has been demonstrated for FCC materials, in which planar slip is often dominant and favors high plastic localization.

Here, we detail a novel dynamic plastic deformation delocalization mechanism that significantly homogenizes plasticity during deformation in FCC solid-solution materials. This mechanism was observed to occur at low levels of plasticity and is therefore relevant to fatigue properties. The underlying small-scale processes of this mechanism and its impact on fatigue strength are examined in detail. The influence of alloy chemistry is demonstrated, revealing a new design space that enables dynamic plastic homogenization, thereby improving fatigue efficiency without compromising monotonic strength.

RESULTS

Plastic localization response in several FCC materials

In order to characterize the plastic localization response of a material at the microstructural level and at low levels of deformation, a statistical and high-resolution approach was employed. High-resolution digital image correlation (HR-DIC) measurements were performed to analyze large fields of view on the order of a square millimeter with a nanometer resolution (*i.e.*, 22 nanometers spatial resolution) to quantitatively capture the characteristics of each deformation event. This combination enables the precise statistical quantification of plastic deformation localization in metallic materials[9,26,27]. Details concerning HR-DIC measurements and mechanical testing procedures are provided in the Methods section and in Supplementary Fig. 1.

HR-DIC measurements were performed after unloading on several solid-solution-strengthened FCC materials, including CrCoNi, CrMnFeCoNi, FeNi36, VCoNi and stainless steel 316L, to quantify their plastic localization behavior at different loading temperatures, including room temperature (300K), liquid nitrogen (77K) and near-liquid helium temperature (20K). All materials were processed to be single-phase FCC solid solutions and to have similar microstructure in terms of grain size, grain shape, and texture. This ensures a direct comparison, as the intensity of plastic localization events is highly dependent on the microstructure[28–31]. The details of these materials and their properties are provided in Table 1 in the Methods section.

We present the (HR-DIC) ϵ_{xx} longitudinal strain maps in Fig. 1 for the CrMnFeCoNi and CrCoNi materials. The electron backscatter diffraction (EBSD) inverse pole figure (IPF) maps, showing the microstructure of these alloys corresponding to the representative regions, have been included in the insets. The IPF maps are colored along the loading direction (horizontal) using color-blind friendly coloring. The high-entropy CrMnFeCoNi alloy, when deformed in tension at room temperature to a macroscopic plastic strain of 0.95%, demonstrates intense plastic localization in the form of discrete deformation events as observed on the corresponding strain map in Fig. 1a. This is further highlighted in the inset focusing on an individual grain within the investigated region. This plastic localization response, characterized by discrete intense deformation events (*i.e.* intense slip localization), is typically observed in FCC materials undergoing deformation at both room and cryogenic temperatures[9,25]. For most of the investigated materials and temperature conditions, we observed a similar response (see Supplementary Fig. 4), consistent with previous reports in the literature[9]. Surprisingly, for the CrMnFeCoNi deformed at liquid nitrogen temperature (77K) and CrCoNi deformed at room temperature to macroscopic plastic strains of 0.83% and 1.66%, respectively, we observed a drastically different plastic localization response. This plastic response was characterized by a homogeneous distribution of plasticity as evidenced by the strain maps presented in Fig. 1b, c. Specific regions showing this homogenized plasticity response have been enlarged in the respective insets, indicating very low-intensity slip localization with plasticity extending over the entire crystallographic grains. The localization is remarkably uniform, rendering it impossible for the HR-DIC approach to capture individual deformation events within these materials. Nevertheless, high average strains are observed within each grain, indicating residual plastic deformation. Additional examples of this plastic response are shown in Supplementary Fig. 5.

Overall, an unusual plastic response in the form of homogeneous plasticity was observed in a few materials under specific testing conditions, thereby differing from the conventional localized plastic response typically exhibited by most investigated FCC metals.

Quantitative measurement of plastic localization

The average plastic localization intensity, measured in nanometers, is presented in Fig. 2a for the investigated FCC solid-solution-strengthened alloys. The materials were subjected to monotonic tensile tests up to a macroscopic plastic strain of ~0.8%. The average plastic localization is a quantitative metric that describes the intensity of plastic localization from individual deformation events. It corresponds to the magnitude of the cumulative Burgers vector projected onto the specimen surface and is extracted using the HR-DIC approach[27], which is detailed in the Methods section. Each deformation event, such as slip or twinning, induces a local displacement (*i.e.*, a step and in-plane displacement) at the specimen surface, which can be quantified using HR-DIC[25]. The intensity of the displacement along the event, representing the in-plane displacement induced by the deformation event, is measured in nanometers. All deformation events (thousands of events) were segmented, and the maximum amplitude along each event was extracted. The

Table 1 | Chemical composition (at.%), grain size (GS) and yield strengths (YS) of the alloys considered in this study

Alloy Denomination	Co (%)	Cr (%)	Ni (%)	Fe (%)	Mn (%)	V (%)	Al (%)	Si (%)	Ti (%)	Mo (%)	C (%)	GS (μm)	YS (RT / LN_2 / LHe) (MPa)
CrCoNi	33.33	33.33	33.33	/	/	/	/	/	/	/	/	25	300 / *500* / **630**
CrMnFeCoNi	20	20	20	20	20	/	/	/	/	/	/	32	200 / *395*
VCoNi	33.33	/	33.33	/	/	33.33	/	/	/	/	/	30	600 / *780*
FeNi36	0.48	0.27	36.59	60.32	0.61	/	0.21	0.81	0.12	/	0.23	27	290 / *630*
316L	0.18	18.71	11.24	65.67	1.71	/	/	0.62	/	1.31	0.1	50	280 / *630*

https://doi.org/10.1038/s41467-026-69046-3

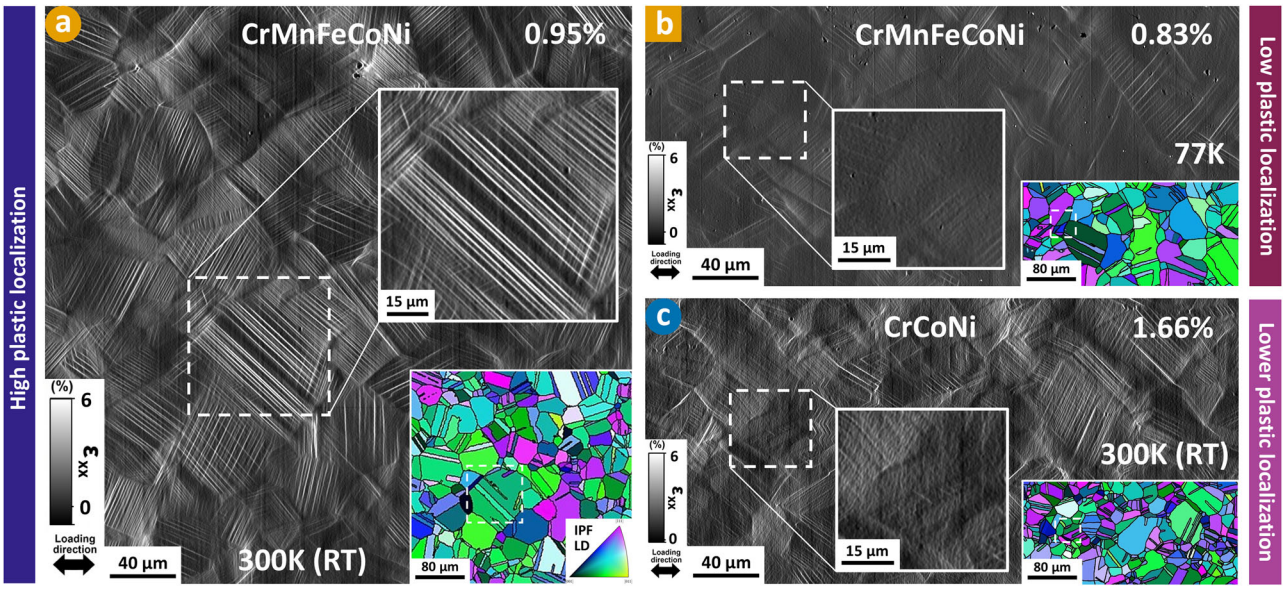

Fig. 1 | A transition from intense plastic localization to more homogeneous plastic deformation. a HR-DIC ϵ_{xx} longitudinal strain maps for CrMnFeCoNi deformed at room temperature (300K) up to a macroscopic plastic strain of 0.95%, (**b**) CrMnFeCoNi deformed at liquid nitrogen temperature (77K) up to a macroscopic plastic strain of 0.83% and (**c**) CrCoNi deformed at room temperature up to a macroscopic plastic strain of 1.66%. The tensile direction is horizontal. The inverse pole figure maps along the loading direction obtained by electron backscatter diffraction corresponding to the HR-DIC maps are displayed in the insets. Reduced regions of interest are denoted using white dashed boxes and enlarged to highlight the differences in plastic deformation localization response across the investigated materials.

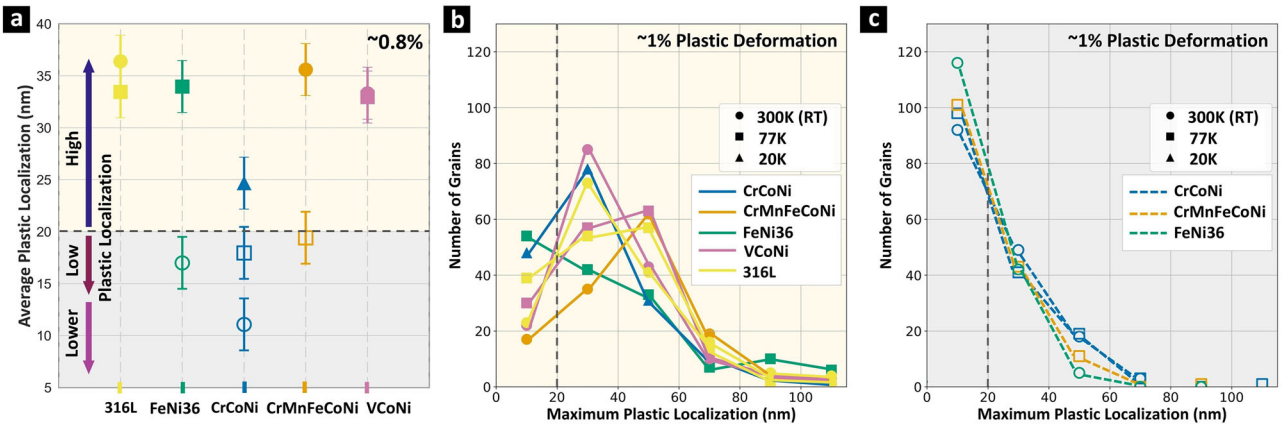

Fig. 2 | Outlier alloys inhibit the intense plastic localization typically observed in conventional alloys. a Average plastic localization in nanometers for several FCC solid-solution-strengthened alloys deformed up to a macroscopic plastic strain of 0.8% at different temperatures. The error bars correspond to experimental variations from HR-DIC measurements. **b**, **c** Distribution of the number of grains as a function of the maximum plastic localization for the investigated materials. Materials that develop intense plastic localization are represented using solid lines and solid symbols (**b**), whereas materials showing diffused, homogeneous plasticity are represented using dashed lines and open symbols (**c**), showcasing a clear difference in the distribution trend between materials showing localized or diffused plasticity. Source data are provided as a Source Data file.

average plastic localization is then defined as the average value of the intensity of all detected events across the entire investigated region (about a square millimeter per material), that includes thousands of deformation events.

We observe that most of the investigated materials exhibit a high average plastic localization. In contrast, CrMnFeCoNi deformed at 77K, FeNi36 deformed at 300K and CrCoNi deformed either at 300K or 77K develop a surprisingly low average plastic localization, with values reduced by almost a factor of two compared to materials that exhibit high plastic localization. We arbitrarily divided the investigated materials into two categories, classified as “High" for the first one (average plastic localization above 20 nm) and “Low" and “Lower" for the second one, represented by yellowish and gray colors, respectively, in Fig. 2a. This background color scheme and denomination will be maintained throughout the manuscript. For the medium-entropy alloy CrCoNi, in particular, the average plastic localization at room temperature is significantly lower, ~three times lower, compared to the other alloys that conventionally localize plasticity. A similar representation for the maximum plastic localization is shown in Supplementary Fig. 6.

For each of the investigated materials at different testing temperatures, the distributions of the number of crystallographic grains as a function of the maximum plastic localization have been represented in Fig. 2b, c. The materials were deformed up to a macroscopic plastic strain of around 1%. The maximum plastic localization is expressed in nanometers and refers to the displacement induced by the most

intense deformation event observed in a particular grain in the investigated representative microstructural region on the surface of the specimen. We observe from Fig. 2b that the materials that show intense plastic localization display a distinct trend compared to the materials that show homogeneous plasticity (*i.e.* low or lower plastic localization) represented in Fig. 2c. For materials that develop intense localization, the distribution of the number of grains as a function of the maximum plastic localization shows peaks above our 20 nm threshold (see dashed black lines in Fig. 2). This displays that most of the considered grains in the investigated regions contain deformation events with a high plastic localization. On the other hand, materials exhibiting homogeneous plasticity (gray region in Fig. 2a) show a clear downward trend in the distribution of grains as a function of the maximum plastic localization. More importantly, they do not show grains with intense plastic localization. For these materials, most grains contain deformation events with extremely low plastic localization values (below our 20 nm threshold, see Fig. 2c) or the plasticity is so diffused that individual deformation events cannot be resolved as discrete events using HR-DIC.

Transmission electron microscopy for characterization of defects

We used HR-DIC ϵ_{xx} longitudinal strain maps to identify specific grains showing either intense plastic localization or homogeneous plasticity for the investigated materials and various testing temperatures. Thin foils were extracted from these locations and conventional transmission electron microscopy (TEM) analysis was performed as shown in Fig. 3. The strain maps corresponding to a reduced region of interest for the medium-entropy alloy VCoNi and high-entropy alloy CrMnFeCoNi deformed at 300K are shown in Fig. 3a, d, respectively. Intense discrete deformation events are evident and the locations of the extracted TEM foils have been highlighted in the grains of interest using pink and orange bands. Bright-field (BF) TEM images primarily reveal the presence of full dislocations across extended areas of the foils, as observed in Fig. 3b, e. Details of regions marked with a white dashed box are presented in Fig. 3c, f, respectively. Although CrMnFeCoNi develops homogeneous plasticity when deformed at 77K (just below our threshold in Fig. 2a), the strain map shows grains with localized plasticity. Within this material, some grains demonstrate low plastic localization, while others show high plastic localization. Additional details on the distribution of the intensity of plastic localization in this material are provided in Supplementary Fig. 6c. A TEM foil was extracted from one grain with intense plastic localization and shown in the inset in Fig. 3g. The corresponding BF TEM image in Fig. 3g reveals a distribution of full dislocations across the foil, similar to what was observed on the room temperature foil for this material. We followed the same approach to characterize the homogeneous plasticity ("Low" or "Lower" plastic localization) exhibited by some materials. The ϵ_{xx} longitudinal strain maps corresponding to FeNi36 deformed at 300K and CrCoNi deformed at 300K are shown in Fig. 3h, k, respectively, along with the location of the extracted foils represented by green and blue bands. The observed plastic responses of the grains of interest differ drastically from the grains shown in Fig. 3a, d and are characterized by homogeneous plasticity. BF TEM images reveal the presence of dislocations across the foil along with a large number of planar defects such as stacking faults, as evidenced from Fig. 3i, l. The regions marked with a white dashed box have been enlarged in Fig. 3j, m, respectively, to further highlight the presence of extensive stacking faults. Another TEM foil extracted from a grain with homogeneous plasticity (low plastic localization) for CrCoNi deformed at 77K is shown in the inset of Fig. 3n. The corresponding BF TEM image captured in Fig. 3n indicates the presence of dislocations as well as a high density of planar defects, similar to our observation on the foil corresponding to CrCoNi deformed at 300K, but with the addition of stacking fault tetrahedron[32–34]. Additional selected-area diffraction pattern comparisons are provided in Supplementary Fig. 7.

Our conventional TEM analysis suggests that materials with homogeneous plasticity during deformation activate a high density of planar defects in addition to full dislocations. Conversely, materials with an intense plastic localization primarily exhibit full dislocations and conventional dislocation pile-up processes[35,36], see also Supplementary Fig. 8.

High-resolution transmission electron microscopy for defect type identification

To further identify the types of defects in the investigated materials, multi-scale characterization using methods of scanning transmission electron microscopy (STEM) down to the atomic-resolution were performed on the different specimens. Detailed parameters used for STEM analysis are provided in the Methods section. A large field-of-view BF-STEM diffraction contrast imaging (DCI) micrograph from a grain exhibiting intense plastic localization in CrMnFeCoNi is shown in Fig. 4a. BF-STEM DCI micrographs from grains displaying homogeneous localization in CrMnFeCoNi and CrCoNi are shown in Fig. 4b, c, respectively. The strain maps associated with the grains from which the foils were extracted are included as insets, with the foil locations indicated by transparent orange or blue bands. The average strains along the loading direction (ϵ_{xx}) of the investigated grains are also shown. In both the low and lower plastic localization cases, residual plastic deformation is present despite the absence of obvious intense deformation events.

Despite a similar average plastic strain in the two investigated grains in the high-entropy alloy CrMnFeCoNi, the defect structures differ significantly. A higher density of defects, slip planes and dislocation debris are observed within the foil extracted from the grain with low plastic localization. In CrCoNi, characterized by the lowest plastic localization (see Fig. 2), the investigated grain shows homogeneous plasticity despite a high level of average plastic strain within the grain of 1.79%. The deformation events display a high density of defects, slip planes and dislocation debris. Interestingly, they also exhibit an extended thickness, as shown in Fig. 4c by the blue dimension line. Within this deformation event, we observed dislocation debris along multiple closely spaced slip planes. This specific structure was present in most of the deformation events within this foil. Dark-field transmission electron microscopy (DF-TEM) images, obtained using two different objective aperture positions from the (lower) delocalizing grain in CrCoNi deformed at room temperature, are shown in Fig. 4d, g. The corresponding selected-area diffraction pattern (SADP) is presented in Fig. 4e, with the objective aperture positions indicated by yellow circles corresponding to images in Fig. 4d, g. The diffraction pattern reveals faint spots associated with deformation twins, and Fig. 4g shows that these twins are extremely small, below the image resolution, and are interestingly of high-density and located solely within the deformation events. Figure 4f shows a 3D view of the SADP corresponding to the orange dashed box in Fig. 4e for better visualization of the faint spots associated with twins. Notably, the atomic scale nanotwins that occur within the extended events do not contribute to the SADP at low magnification, with additional diffraction spots appearing when focusing on extended deformation events.

Atomic-resolution HAADF-STEM images from within deformation events in the medium-entropy alloy CrCoNi deformed at room temperature, shown in Fig. 5g, reveal the presence of several nanometer-scale deformation twins and other planar defects, such as intrinsic stacking faults. Center of Symmetry (COS) analysis[37,38], which measures the degree of centro-symmetry for each atomic column in the experimental HAADF-STEM image, was performed to identify distortions in the stacking sequence. The results, displayed in Fig. 5h,

https://doi.org/10.1038/s41467-026-69046-3

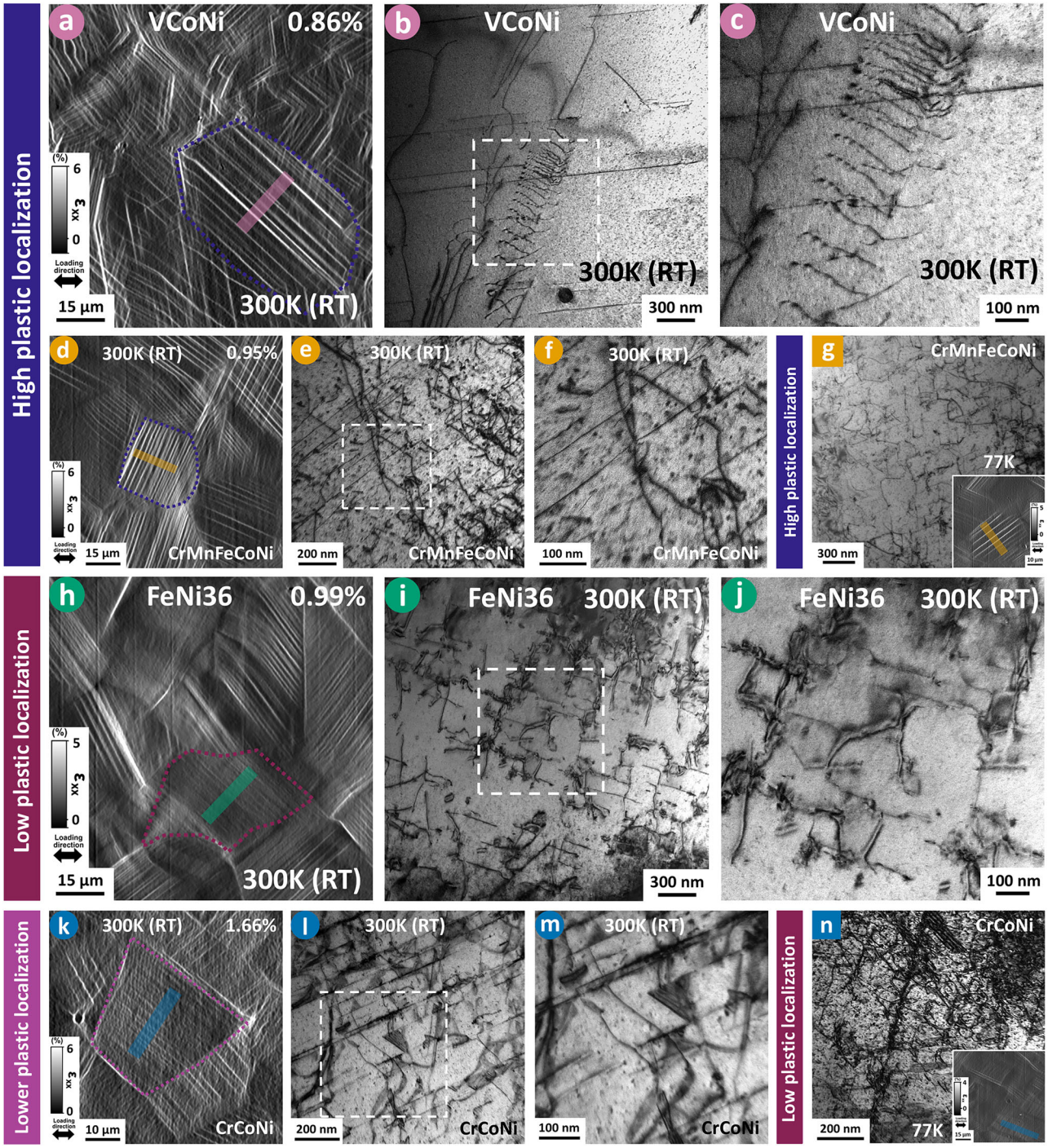

Fig. 3 | Planar defects are observed to promote plastic homogenization. Reduced regions of the HR-DIC ϵ_{xx} longitudinal strain maps for (**a**) VCoNi deformed at room temperature, (**d**) CrMnFeCoNi deformed at room temperature, (**h**) FeNi36 deformed at room temperature, and (**k**) CrCoNi deformed at room temperature. The macroscopic plastic strains up to which the materials were deformed are included on the respective HR-DIC maps. Grains developing intense plastic localization and diffused plasticity were selected and TEM foils were extracted, marked as colored bands in (**a**, **d**, **h**, **k**). Bright-field (BF) TEM images for the foils marked in (**a**, **d**) primarily reveal the presence of full dislocations across the foils (**b**, **e**), whereas planar defects such as stacking faults are observed (**i**, **l**) for the foils marked in (**h**, **k**). Regions marked with white dashed boxes in (**b**, **e**, **i**, **l**) have been enlarged in (**c**, **f**, **j**, **m**) respectively. Additional TEM foils extracted for different testing temperatures are shown in the insets in (**g**) and (**n**). The corresponding BF TEM images show full dislocations and additional planar defects for localizing and diffused plasticity grains, respectively (**g**, **n**).

confirm the presence of several nanometer-scale deformation twins within the observed deformation event in addition to intrinsic stacking faults. Additional examples provided in Supplementary Figs. 9 and 10 demonstrate that this defect structure was consistently observed across all investigated deformation events in CrCoNi deformed at room temperature.

Similar imaging and analysis were conducted on CrCoNi deformed at 77 K on a crystallographic grain which exhibits homogeneous plastic localization (low plastic localization), but with a slightly higher plasticity localization when compared to the same alloy tested at room temperature (lower plastic localization). In this case, as shown in Fig. 5d and e, within the deformation event, we detect only

https://doi.org/10.1038/s41467-026-69046-3

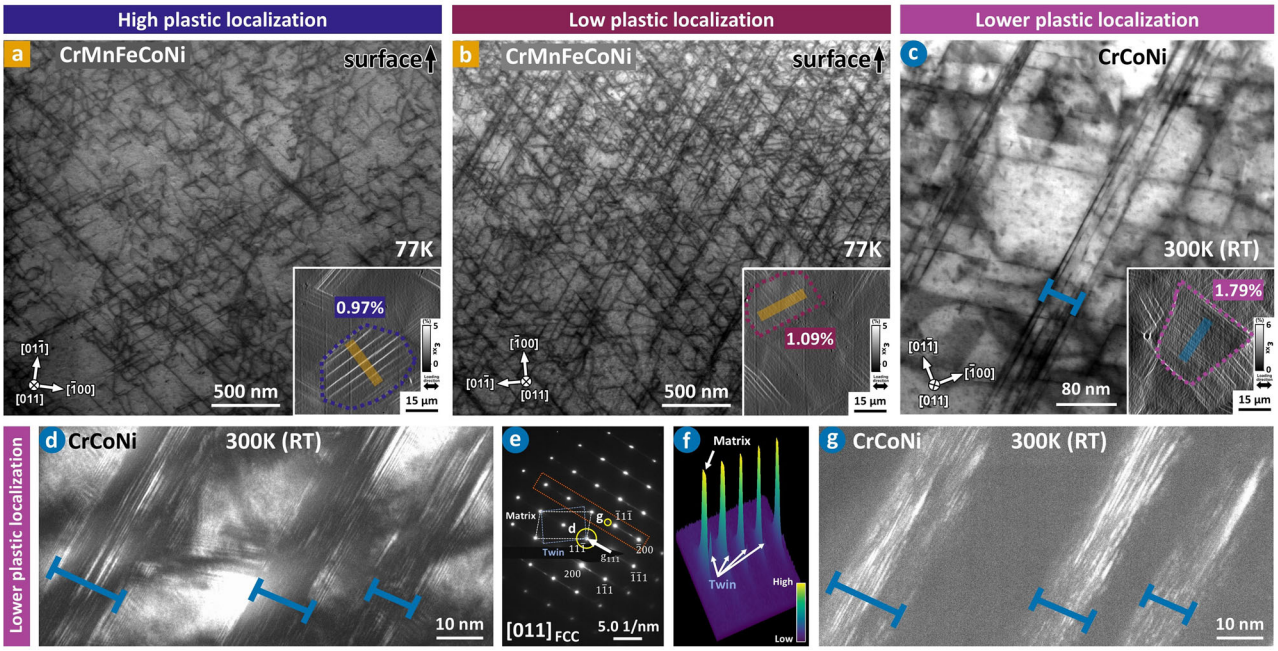

Fig. 4 | A high density of nanoscale twins promotes reduced plastic localization through the formation of closely spaced slip events. BF-STEM DCI micrographs from (**a**) a (high) localizing grain for CrMnFeCoNi deformed at 77K, (**b**) a (low) delocalizing grain for CrMnFeCoNi deformed at 77K and (**c**) a (lower) delocalizing grain for CrCoNi deformed at 300K. The figure insets display reduced regions of the HR-DIC ϵ_{xx} longitudinal strain maps showing the grains from which thin foils were extracted along with the average strain in the considered grains. **d**, **g** DF-TEM images from the (lower) delocalizing grain in (**c**). **e** Corresponding SADP for the grain in (**c**), with locations of the objective aperture used to capture DF-TEM images in (**d**, **g**) shown by yellow circles. **f** shows a 3D view of the SADP corresponding to the orange dashed box in (**e**). The electron beam is parallel with the [011] crystallographic zone axis of the investigated grains.

extended planar defects consisting of intrinsic and extrinsic stacking faults, hexagonal close-packed (HCP) structures, stacking fault tetrahedra, and extended deformation twinning (see Supplementary Fig. 7). However, no nanometer-scale deformation twins were detected. Finally, in the foil extracted from the grain exhibiting intense localization, no extended planar defects were identified within the deformation events, as shown in Supplementary Fig. 8.

A dynamic delocalization mechanism: the role of stacking fault energy

We calculated the stacking fault energies (SFE), which represent the energy per unit area associated with the formation of a stacking fault, as a function of temperature for CrCoNi, CrMnFeCoNi, FeNi36, and VCoNi. The SFE for stainless steel 316L was not calculated due to its complex atomic arrangement. The calculation method is detailed in the Methods section and is based on density functional theory (DFT) and ab-initio molecular dynamics (AIMD) to estimate stacking fault energies at 0K and finite temperatures, respectively. Figure 6a shows a schematic of an intrinsic stacking fault and the corresponding partial Burgers vector. An example of the SFE calculation at 0K is shown in Fig. 6b for the medium-entropy alloy VCoNi, highlighting the variation in calculated SFE values for different slip-cut configurations. These variations were also found in other FCC multi-component alloys[39–42]. They cause local stacking fault and critical resolved shear stress variations, and the maximum local stress dictates the macroscopic deformation[43,44]. To estimate the stacking fault energy at finite temperatures, the slip-cut corresponding to the maximum SFE at 0K is chosen, as shown in Fig. 6c. The maximum SFE corresponds to the maximum resolved shear stress that needs to be overcome for dislocation glide. Finally, Fig. 6d presents the calculated stacking fault energies as a function of temperature for the investigated materials. VCoNi[45] and FeNi36 both exhibit increasing stacking fault energy with decreasing temperature, whereas CrMnFeCoNi and CrCoNi show the opposite trend[46]. This is due to preference of HCP stability by Co, Cr, and Mn elements such that high d-electron density around Fermi level easily reacts on stacking fault formation at low temperature[47,48], while V and Fe promote FCC stability.

We summarize both the HR-DIC and S/TEM analyses in Fig. 7a. We observe that the presence of nanometer-scale planar defects within deformation events significantly reduces plastic localization. In the case of nanometer-scale deformation twins, plastic localization is even more strongly suppressed. Above of our plastic localization threshold, we only observed the presence of full dislocations (high stacking fault energy) or long deformation twins (low staking fault energy case for the CrCoNi deformed at 20K and detailed later in Fig. 8) that promote the usual intense plastic localization observed in metallic materials[9,36]. The simplistic schematic of the conventional deformation processes occurring in FCC materials at both room and low temperatures is illustrated in Fig. 7b. These processes typically involve planar slip, for which a large number of dislocation events glide along a given crystallographic plane and emerge at the surface, thus leading to large surface steps and resulting in an intense localization[9,36]. Similarly, when deformation twinning dominates, large and extended twins form, producing significant surface steps associated with an intense localization.

Figure 7d shows the average plastic localization for the investigated materials and various temperature conditions as a function of the calculated SFE at each temperature. The background color scheme in Fig. 7d matches that of Fig. 2a, where materials and testing conditions that exhibit low plastic localization (below our threshold) are shown on a gray background. We observe that all the materials and testing conditions exhibiting low plastic localization, indicative of plastic homogenization, fall within a narrow range of intermediate SFE values. For materials with high SFE, our S/TEM analyses revealed that deformation is primarily dominated by full dislocations. In contrast, for CrCoNi deformed at 20K, we observed the formation of extended deformation twins. CrCoNi deformed at room temperature, which exhibits the lowest level of plastic localization, falls within the middle

https://doi.org/10.1038/s41467-026-69046-3

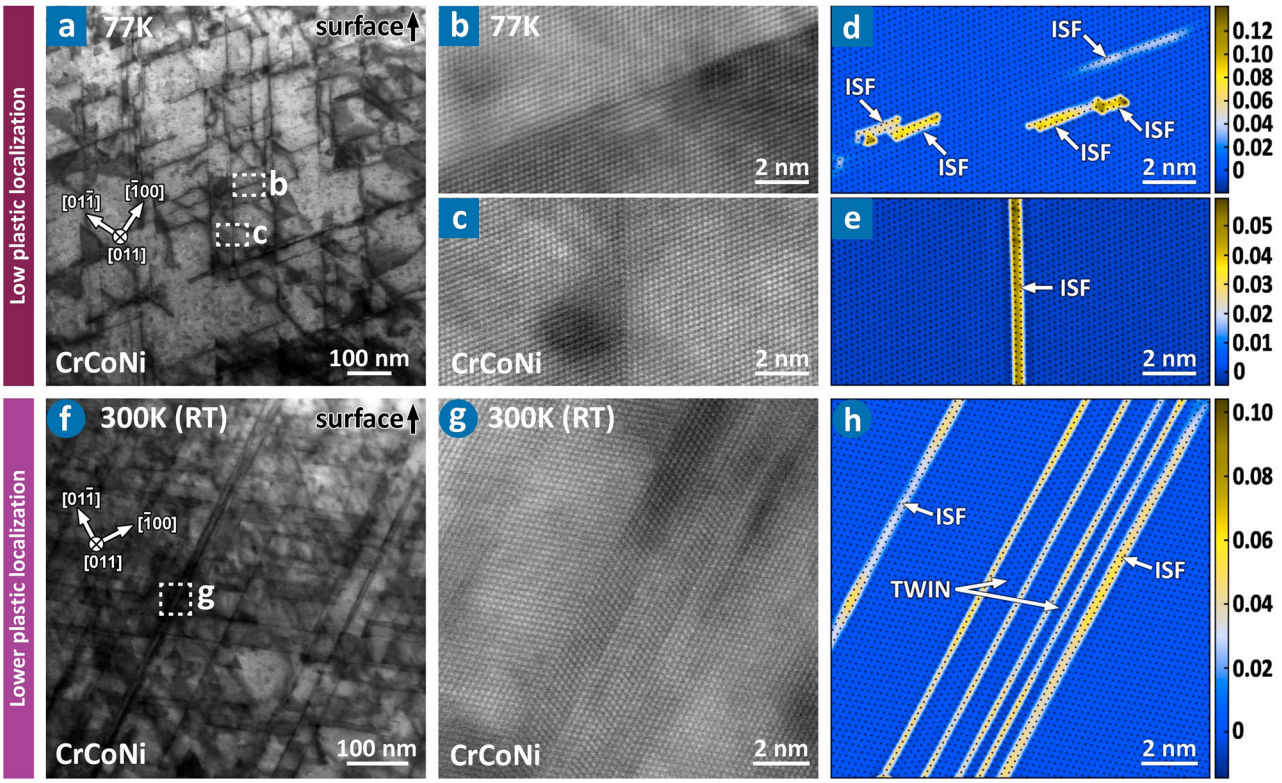

Fig. 5 | Atomic-resolution imaging reveals small-scale planar defects within deformation events where delocalization occurs. a BF-STEM DCI micrograph from a (low) delocalizing grain for the CrCoNi alloy deformed at 77K. **b**, **c** Atomic resolution HAADF-STEM images within two deformation events from (**a**). **d**, **e** Associated center of symmetry analysis. **f** BF-STEM DCI micrograph from a (lower) delocalizing grain for the CrCoNi alloy deformed at room temperature. **g** Atomic resolution HAADF-STEM image within a deformation event from (**f**). **h** Associated center of symmetry analysis. The colorbar shows the range of center of symmetry parameter values (dimensionless) calculated for atomic column positions in the analyzed area. The electron beam is parallel with the [011] crystallographic zone axis of the investigated grains.

of the narrow region of intermediate SFE values. In this case, deformation events are characterized by large thicknesses (closely spaced slip bands) and contain a high density of nanometer-scale deformation twins and full dislocations. The underlying mechanisms are simplistically schematically illustrated in Fig. 7c.

These nanometer-scale twins, which were not present prior to deformation are observed to form during deformation and influence dislocation glide by forcing dislocations to glide on closely spaced crystallographic planes, as observed in Fig. 4c. This suggests a dynamic mechanism that promotes plastic homogenization through the competition and interaction between nanometer-scale deformation twins and full dislocation glide. We had initially observed evidences of this plastic homogenization phenomenon through closely-spaced slip in a previous study investigating the precipitation strengthened nickel based superalloy Inconel 718 at ambient and cryogenic temperatures[25]. At cryogenic temperatures (77K and 9K), deformation events consisted of multiple closely spaced slip traces, with detailed atomic resolution HAADF-STEM analysis revealing the presence of nanoscale planar defects such as intrinsic and extrinsic stacking faults, twins and HCP regions in the vicinity of these multiple slip events.

The mechanism at play is not the formation of nanotwins during deformation, which has been previously observed in FCC metals[37,38,49], but rather the interaction between dislocation glide and nanotwins, and its resulting effect on the intensity of plastic localization. The observed behavior in plastic localization may be explained by two potential deformation mechanisms. The first involves the role of planar defects such as nanotwins in promoting cross-slip, as suggested in references[50,51]. However, materials with low stacking fault energy usually suppress cross-slip and favor planar slip. A second possible mechanism involves the activation or deactivation of dislocation sources. A recent study on CrCoNi under room-temperature compression[52] demonstrated that the formation of extended stacking faults in FCC materials can deactivate dislocation sources. Atomistic simulations showed that when the leading partial dislocation has a higher Schmid factor than the trailing one, it glides first, forming a stacking fault. However, the trailing partial remains inactive, resulting in an unstable configuration that increases the energy barrier for further glide. This leads to source deactivation after emitting a single partial, deviating from the conventional Frank-Read dislocation multiplication model[53]. Moreover, twin boundary migration induced by partial dislocation glide may create additional dislocation sources at stacking fault-twin boundary interfaces. This will promote dislocation glide on successive planes, ultimately forming the closely spaced slip bands we observed. Finally, some of the investigated alloys, such as CrCoNi, VCoNi, and CrMnFeCoNi, may exhibit short-range ordering (SRO)[54,55], which could influence the previously discussed mechanisms. SRO can promote partial-dislocation-mediated plasticity processes, including stacking fault formation, twinning, and HCP phase nucleation, leading to the generation of deformation debris that refines the microstructure while introducing additional obstacles to dislocation motion[40–42,56,57]. Chemical fluctuation such as SRO was also observed to promote or inhibit cross-slip[57–61]. These processes may therefore also contribute in promoting or inhibiting the phenomenon of dynamic plastic delocalization. However, SRO is not a necessary condition for such behavior, as plastic delocalization is also observed in the binary FeNi36 alloy, which exhibits weak SRO and mechanical properties largely unaffected by it[62]. Moreover, SRO in CrCoNi and CrMnFeCoNi has been observed to have no noticeable effect on

https://doi.org/10.1038/s41467-026-69046-3

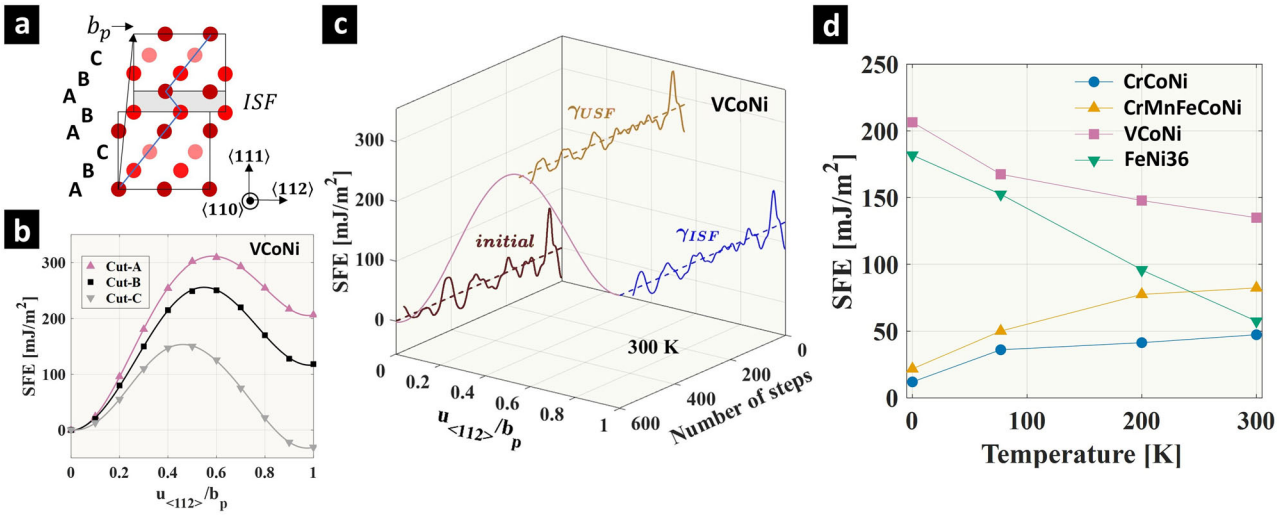

Fig. 6 | Stacking fault energy calculations to inform planar defects formation. **a** Schematic of stacking fault energy (SFE) calculation upon slip; Partial burgers vector (b_p) along < 112 > direction is applied at intrinsic stacking fault (ISF) point; Stacking sequence (such as ABCABABC) is denoted after slip. **b** Example of SFEs in random VCoNi alloy at 0 K based on density functional theory (DFT); Different slip-cut configurations result in SFE variation. **c** Example of SFE of VCoNi alloy using ab-initio molecular dynamics (AIMD) at 300K; The slip-cut where the maximum SFE is shown at 0 K is chosen (such as Cut-A in (**b**)). **d** SFE variation as a function of temperature for different alloys in this study. Source data are provided as a Source Data file.

macroscopic properties and therefore may not be an influential factor on the identified mechanisms[63,64].

To further demonstrate that nanoscale planar defects, including nanotwins with a thickness limited to a few atomic planes (less than 5 nm) and their interaction with dislocation glide are the deformation mechanisms responsible for dynamic plastic delocalization, we suppressed these interactions by promoting the formation of extended twins having thicknesses in the range of several tens to hundreds of nanometers (thereby preventing the effect of nanoscale planar defects, including nanotwins) and subsequently examined the resulting plastic localization. Specifically, we analyzed CrCoNi deformed at 20K, which exhibits low SFE, as well as CrCoNi deformed at 77K under high levels of plastic strain to promote the formation of extended twins.

CrCoNi deformed at 20K exhibits significant plastic localization, as shown in Fig. 2a, indicating that dynamic plastic delocalization is not active at this temperature, unlike at room temperature and 77K. Figure 8a presents the distribution of plastic localization amplitudes for different applied plastic strains. These distributions include all deformation events within the investigated regions, where the maximum value for each event is used. For a given applied plastic strain, CrCoNi shows markedly lower localization when dynamic plastic delocalization occurs, as previously reported in Fig. 2a, while strong localization is evident at 20K. Examination of the deformation substructure of CrCoNi deformed at 20K associated with intense events (Fig. 8f–i) reveals extended deformation twins with thicknesses of several tens to hundreds of nanometers, contrasting with the few-nanometer-thick twins observed in CrCoNi deformed at room temperature, where dynamic plastic delocalization is activated (see Fig. 5h). SFE calculated at 20K is lower, consistent with the presence of extended deformation twins. This further supports that dynamic plastic delocalization occurs within a narrow SFE window between low and high SFE values. To reinforce the link between extended deformation twinning, plastic localization, and the suppression of dynamic plastic delocalization, CrCoNi was deformed at 77K to a higher strain of about 4.6%. The corresponding distribution of plastic deformation events (Fig. 8a) reveals intense localization (see also Fig. 8c). The evolution of event intensity with applied strain for CrCoNi deformed at 77K deviates from the linear trend observed at lower deformation levels (dashed lines in Fig. 8a), indicating a transition to a different deformation regime. High-resolution EBSD analysis confirms the presence of extended deformation twins with thicknesses up to several hundred nanometers (Fig. 8d). Further advanced analysis resulting from encoding of electron backscatter diffraction Kikuchi patterns (Fig. 8e), detailed in the Methods section, reveals that these deformation twins extend along the full length of deformation events, offering finer detail than the conventional EBSD map alone. Once again, such extended twins are associated with pronounced plastic localization and the suppression of dynamic plastic delocalization. With increasing strain or decreasing SFE, CrCoNi thus favors the formation of extended deformation twins, which hinder dynamic plastic delocalization and promote strong plastic localization.

A new design space for enhancing fatigue strength

The influence of the identified dynamic plastic deformation delocalization mechanism on fatigue properties was evaluated by measuring the fatigue strength of CrCoNi, CrMnFeCoNi, and 316L stainless steel at room temperature in the very high cycle fatigue (VHCF) regime. Stainless steel served as a reference material due to its conventional plastic localization behavior. Among the tested alloys, CrMnFeCoNi exhibits the highest degree of plastic localization, while CrCoNi shows the lowest. The tendency of an FCC material to localize plastic deformation is known to correlate with its fatigue performance[9]; materials exhibiting intense localization typically demonstrate lower fatigue ratios, defined as the fatigue strength divided by the yield strength, following the work proposed by Fleck, Kang, and Ashby[15]. In agreement with the consideration that low plastic localization enhances fatigue properties, prior studies have reported superior fatigue performance for CrCoNi compared to CrMnFeCoNi at room temperature[65,66]. However, these comparisons must be contextualized, as those studies primarily addressed low-cycle fatigue (LCF) under relatively high strain amplitudes, where alternative deformation structures such as dislocation cells and vein patterns may dominate the fatigue response[67,68]. In the present study, fatigue performance in the VHCF regime is further compared with literature data for recrystallized FCC alloys tested under similar conditions[66,69–73]. The fatigue life of CrCoNi, CrMnFeCoNi, and 316L stainless steel at room temperature, plotted as a function of maximum applied stress (normalized by their yield strength), is shown in Fig. 9a. Horizontal arrows indicate

https://doi.org/10.1038/s41467-026-69046-3

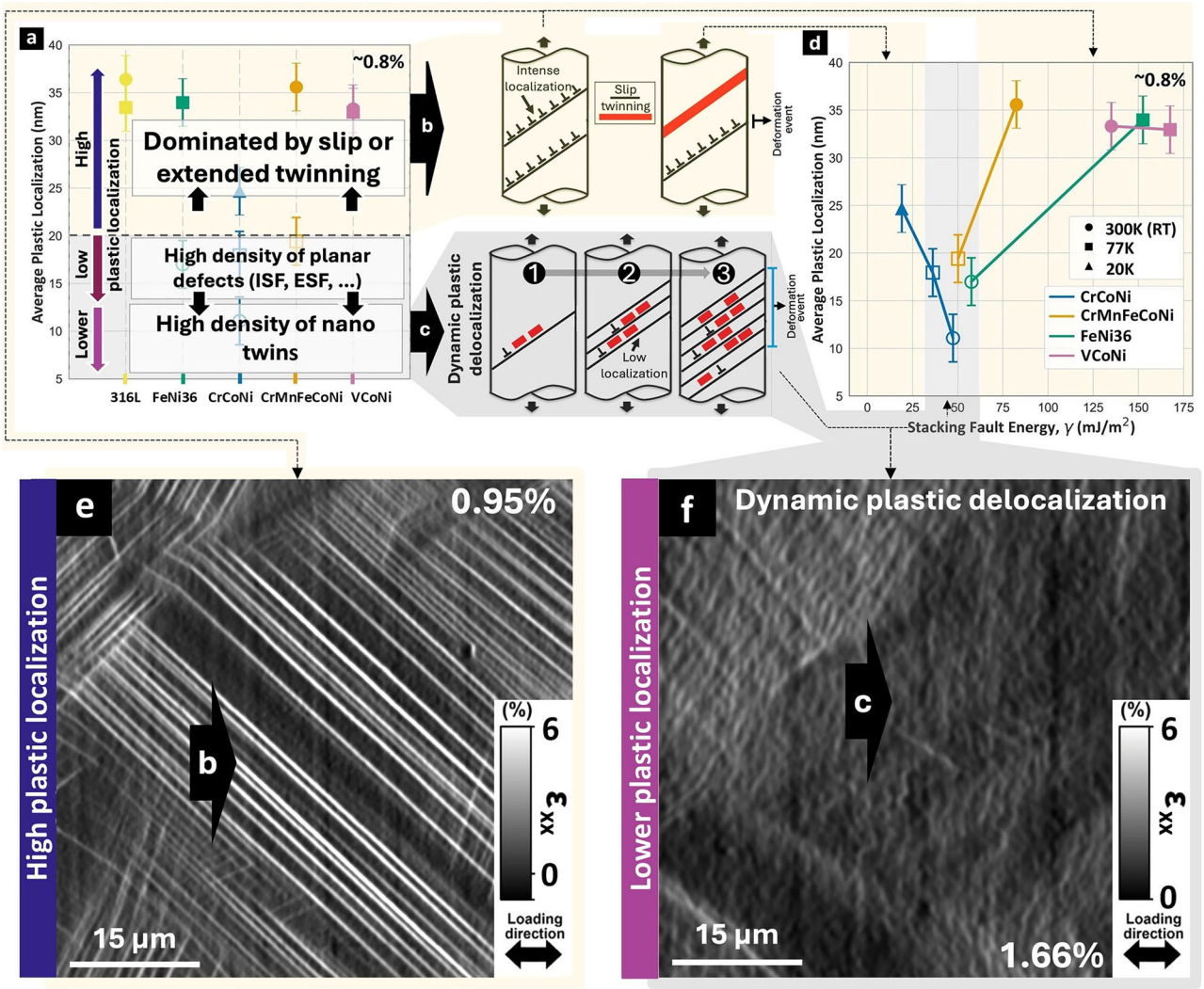

Fig. 7 | A dynamic plastic deformation delocalization mechanism to homogenize metal plasticity. a Observed variations in average plastic localization for several FCC solid-solution-strengthened alloys deformed at a macroscopic plastic strain of 0.8% (reproduced from Fig. 2a). Three distinct regimes were identified: one exhibiting intense plastic localization (labeled as "High"), another showing reduced plastic localization (labeled as "Low"), and a third characterized by a very low level of plastic localization (labeled as "Lower"). The latter two regimes are associated with the formation of planar defects, with the third regime further distinguished by a high density of nanometer-scale twins. **b** Conventional plastic localization processes involving either dislocation glide along specific slip planes or extended deformation twins were observed in the regime with intense plastic localization. **c** The proposed mechanism responsible for the reduced plastic localization amplitude involves the dynamic formation of nanometer-scale twins, which contribute to the thickening of deformation events. **d** The average plastic localization is shown as a function of the stacking fault energy of the alloys at the testing temperatures. The dynamic mechanism that results in a very low level of plastic localization occurs for alloys and temperature conditions within an intermediate range of stacking fault energies. **e**, **f** Examples of HR-DIC ϵ_{xx} longitudinal strain maps for intense plastic localization and homogeneous plasticity, respectively. Source data are provided as a Source Data file.

specimens that did not fail. CrCoNi demonstrates significantly higher fatigue strength compared to CrMnFeCoNi and 316L stainless steel. Figure 9b displays the measured fatigue ratios as a function of the yield strength. A general trend of decreasing fatigue ratio with increasing yield strength is typically observed for FCC metals at room temperature[9]. However, CrCoNi appears as a clear positive outlier, exhibiting a significantly higher fatigue ratio than expected. These findings highlight the beneficial role of dynamic plastic deformation delocalization in enhancing fatigue properties and suggest a transformative design strategy for the development of fatigue-resistant alloys.

Dynamic plastic delocalization occurs in a regime dominated by nanoscale defects and dislocation glide, typically observed at low deformation levels. As deformation increases, twinning becomes more prevalent, with the formation of extended deformation twins that promote intense plastic localization. Consequently, a transition is observed, from a regime where dynamic plastic delocalization enhances fatigue performance (breaks the trade-off between monotonic strength and fatigue strength[9]) to one dominated by the well-known dynamic Hall-Petch effect (breaks the trade-off between strength and ductility), where extended twinning contributes to strain hardening[74–76].

METHODS

Materials

Five different face centered cubic (FCC) solid-solution-strengthened alloys were investigated in this study, namely CrCoNi, CrMnFeCoNi, VCoNi, FeNi36 and stainless steel 316L. For CrCoNi, CrMnFeCoNi and VCoNi, the pure elements were vacuum induction melted and cast into ingots. The ingots were homogenized at 1200 °C for 48 h, followed by rotary swaging for diameter reduction. Recrystallization heat treatments were carried out at 1080 °C for 1 h, 1060°C for 1 h and 1100°C for

https://doi.org/10.1038/s41467-026-69046-3

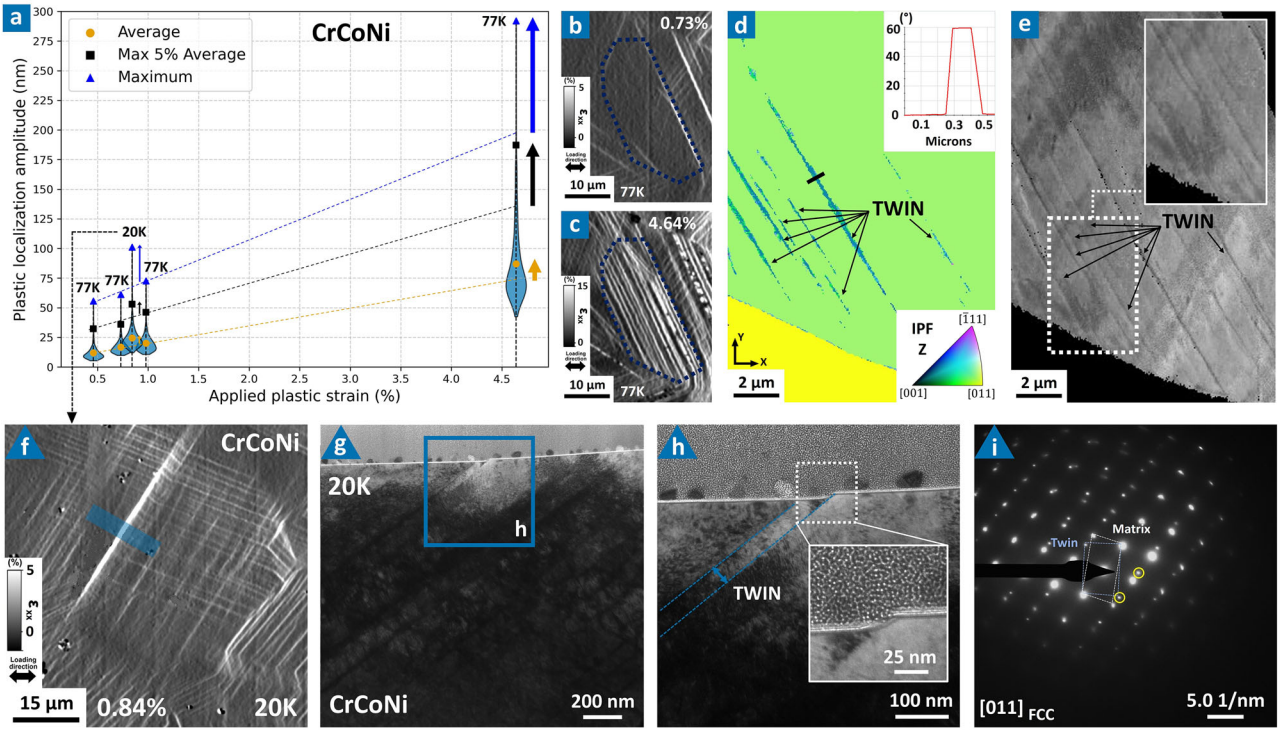

Fig. 8 | Effect of high deformation and lower stacking fault energy promoting intense plastic localization. a Distributions of the plastic localization amplitude as a function of the applied plastic strain for CrCoNi deformed at 77K and 20K. The average localization amplitude, the average of the 5% most intense deformation events and the maximum localization have been shown using orange circles, black squares and blue triangles, respectively. Source data are provided as a Source Data file. Reduced regions of HR-DIC ϵ_{xx} strain maps with the grain of interest marked for CrCoNi deformed at 77K corresponding to macroscopic plastic strains of (**b**) 0.73% and (**c**) 4.64%. **d** EBSD inverse pole figure map along the normal (z) direction indexed using the dictionary indexation approach. The misorientation profile across a deformation twin along the black line is shown in the inset. X indicates the loading direction. **e** Latent space feature map resulting from the encoding of electron backscatter diffraction pattern and revealing thin deformation twins. **f** Reduced region of the HR-DIC ϵ_{xx} strain map for CrCoNi deformed at 20K. The location of the extracted TEM foil is marked with a blue band. **g** BF-TEM overview image of the corresponding TEM foil. An enlarged view of the region marked using a blue box in (**g**) is shown in (**h**). The inset shows the surface step formed due to localized plastic deformation. **i** SADP revealing the presence of an extended deformation twin. The electron beam was parallel with the [011] crystallographic zone axis.

15 minutes for CrCoNi, CrMnFeCoNi and VCoNi, respectively, after which tensile specimens were extracted. 316L specimens were extracted from a water quenched rolled plate, subjected to an annealing treatment at 1055 °C for 1 h under high vacuum, followed by water quenching. FeNi36 specimens were taken from a forged plate subjected to an annealing treatment at 825 °C for 90 minutes followed by air cooling. The chemical composition of the investigated alloys in atomic percent along with the grain size after processing are listed in Table 1. The grain size includes annealing twins. The yield strengths of the alloys at liquid nitrogen and liquid helium temperature are shown using italic and bold formatting, respectively.

Electron microscopy

Scanning electron microscopy (SEM) characterization was performed using a Thermo Fisher Scientific™ Scios 2 Dual Beam SEM/FIB with a field emission gun (FEG). The imaging was conducted over areas with dimensions of 723 × 405 µm^2, using a 6 × 5 grid pattern with 15 % overlap between neighboring images. The imaging was performed at an accelerating voltage of 10 kV and a current of 0.80 nA. Secondary electron images were acquired with a dwell time of 10 µs per pixel, a horizontal field of view of 138 µm and at a working distance of 5 mm. The resulting images have a resolution of 6144 px × 4096 px. Automated imaging was performed using the AutoScript software from ThermoFisher™ and a custom Python routine for automated focus/astigmatism and grid imaging before and after deformation. The Python routine has been made available on GitHub (https://github.com/cmbean2/Automated-SEM-Procedure).

Conventional Electron backscatter diffraction (EBSD) measurements were conducted at a 70° tilt using a step size of 1 micron, square grid collection, 200 frames per second acquisition, an accelerating voltage of 30 kV and a current of 6.4 nA. All EBSD scans were performed prior to deformation on the same regions investigated by HR-DIC. EBSD was performed on a ThermoFisher Scientific Scios 2 Dual Beam SEM/FIB using a Hikari Super EBSD detector. EBSD maps were then adjusted by distortion to match HR-DIC with pixel resolution using the method described in reference[77]. For EBSD scans, confidence index (CI) of 0.5 and higher was obtained.

Energy-dispersive X-ray spectroscopy (EDX) measurements were conducted in a ThermoFisher Scientific Scios 2 Dual Beam SEM/FIB using an Octane Elite silicon drift detector (SDD). The measurements were performed at an accelerating voltage of 20 kV, current of 0.2 nA, working distance of 10 mm, horizontal field of view of 138 µm, 32 frames per second acquisition and a dwell time of 200 µs. The associated results obtained from EDX measurements are provided in Supplementary Fig. 3 and Supplementary Table 1 and 2.

The deformation processes and the profiles of slip step that develop during deformation on the surface were observed and documented with the underlying microstructure using site- and orientation-specific TEM surface lamella preparation by focused ion beam (FIB). A ThermoFisher Scientific Helios SEM-FIB Dual-Beam system was used to extract the thin foils with a final cleaning at 5 kV and a current of 16 pA to minimize beam damage effects and ensure minimal introduction of defects due to sample preparation by FIB. All foils were extracted using the same parameters for consistent comparison across materials and

https://doi.org/10.1038/s41467-026-69046-3

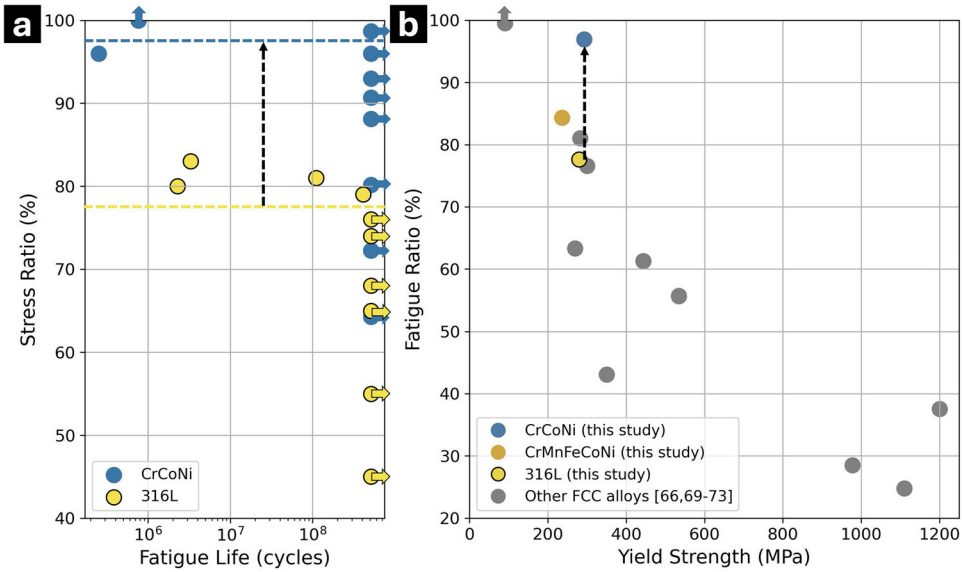

Fig. 9 | Effect of dynamic plastic deformation delocalization on fatigue performance. a Fatigue life at room temperature of the investigated CrCoNi, CrMnFeCoNi alloys, and 316L stainless steel as a function of the maximum applied stress in the very high cycle fatigue regime. The maximum stress is expressed as a percentage of the yield strength. **b** Fatigue strength at room temperature, reported as a percentage of the yield strength (fatigue ratio), plotted against the yield strength for the investigated alloys and additional FCC alloys reported in the literature[66,69–73]. Horizontal arrows indicate specimens that did not fail. Vertical arrows indicate cases where the fatigue life or fatigue ratio exceeds the yield strength of the material. Source data are provided as a Source Data file.

testing conditions. A ThermoFisher Scientific Talos F200X G2 Scanning Transmission Electron Microscope (S/TEM) was used to capture conventional bright-field (BF) and dark-field (DF) TEM images of the different defects developing in these foils. Microstructure and defect analysis from these foils down to atomic resolution were performed using image aberration-corrected and monochromated ThermoFisher Scientific Titan-Themis STEM at an acceleration voltage of 300 kV. STEM diffraction contrast imaging (DCI) was performed with bright (BF) and high-angle annular dark-field (HAADF) detectors by selection of the appropriate camera length[78]. Atomic resolution of the microstructure was performed by tilting the thin foils into specific low-index crystallographic zones. Data was collected and processed using ThermoFisher Scientific Velox software. STEM micrographs were corrected for potential sample drift and scanning beam distortions using the drift-corrected frame integration function of Velox. Center of Symmetry (COS) analysis, which determines the degree of centrosymmetry for each atomic column in the experimental HAADF-STEM image and thus identifies distortions in the stacking sequence, was performed according to the procedure described in refs. 37,38. The dimensionless center of symmetry parameter M_n is calculated for each atomic column as $M_n = \left(\frac{1}{2}\sum_{r=1}^{6} D_r\right) / \left(2\sum_{r=1}^{6} |\mathbf{d}_r|^2\right)$, where $\mathbf{d}_r$ is the relative position vector of one of the six nearest neighbors, ranked by distance (r = 1 to 6), and D_r are the minimum vector sums defined as $D_r = |\mathbf{d}_1 - \mathbf{d}_j|^2$. For more details, see reference[79]. The differentiation between extrinsic stacking faults (ESF) and twin stacking is based on the description used in reference[80].

High-resolution digital image correlation

Before deformation, a speckle pattern consisting of 60 nm silver nanoparticles was formed on the surface of the sample, following the procedure developed by Montgomery et al.[81]. HR-DIC was performed upon completion of each step using proprietary software, XCorrel[27]. HR-DIC images were captured before loading and after unloading for subsequent analysis. The SEM images (6144 px × 4096 px) were divided into subsets of 31 × 31 pixels (700 nm × 700 nm) with an overlap of 28 pixels between each subset (*i.e.*, step size of 3 pixels (67 nm)). A representative scanning electron image of the speckle pattern has been included in Supplementary Fig. 1. Heaviside digital image correlation (H-DIC) is used when considering displacement fields that involve discontinuous displacement, like those produced by slip localizations[82]. Compared to conventional DIC, H-DIC provides higher displacement resolutions below 10 nm and the ability to find multiple discontinuities within a subset. Here, H-DIC enabled direct measurement of the amplitudes of the slip localizations[26,27].

Deformation twinning identification through ML-driven diffraction analysis and dictionary indexation

To identify deformation twinning beyond what is possible with conventional TEM methods, which are typically restricted to specific regions of a specimen (not statistically representative), we employed a complementary set of EBSD-based techniques. Standard EBSD analysis relying on Hough transforms struggles to detect thin deformation twins. The electron interaction volume frequently contains overlapping diffraction patterns from the parent grain and the thin deformation twins, resulting in diffraction patterns that superimpose two or more orientations. Hough-based indexing is not adapted to identify overlapping patterns. To enhance the detection of small deformation twins, we used the dictionary indexing (DI), based on spherical indexing, approach developed in reference[83]. Rather than extracting only band positions, DI leverages the entire diffraction pattern image, using all pixels to achieve more robust orientation determination[84]. A physics-based forward model is used to generate a master Kikuchi pattern, followed by a precomputed dictionary of simulated patterns. For each experimental pattern, a normalized dot product similarity metric is computed against the dictionary to identify the closest match and its corresponding orientation. By exploiting the full angular intensity information in each pattern, DI exhibits improved sensitivity to overlapping patterns and therefore enables a better detection of deformation twins. For the present measurements, an accelerating voltage of 20 kV, a step size of 50 nm and a working distance of 14 mm were used. The spherical indexing used a bandwidth of 53.

Although DI significantly improves the sensitivity of deformation twin detection, it still does not explicitly separate overlapping diffraction patterns from twins and parent grains, which limits its ultimate resolving capability. To further enhance sensitivity, we applied a

machine-learning based approach that relies on diffraction pattern encoding and latent-space feature mapping, as detailed in reference[85]. In this method, a variational autoencoder (VAE) is used to encode the full Kikuchi pattern into a compact low-dimensional representation. Differences in latent-space features directly reveal subtle discrepancies in the diffraction signal. As a result, locations where overlapping twin and parent grain patterns are present become readily distinguishable from those corresponding to the parent grain alone. This approach provides sub-pixel sensitivity to deformation-induced orientation changes, enabling a reliable detection of twins with thicknesses on the order of only a few tens of nanometers. For the present measurements, an accelerating voltage of 20 kV, a step size of 50 nm and a working distance of 14 mm were used. The VAE operates directly on the raw diffraction patterns, without background subtraction, and encodes them into a 128-dimensional latent space.

Mechanical testing

Flat dogbone-shaped specimens with a gauge section of 1×3 mm^2 were machined by electrical discharge machining (EDM) with gauge lengths of either 6 mm or 10 mm. These samples were mechanically tested on a NewTec Scientific™ MT1000 5000 Newton tensile stage and an electromechanical 3R™ VHCF MEG20TT frame equipped with a custom setup for cryogenic testing. The cooling system consists of a vacuum double-walled chamber, multilayer insulation material, and helium/nitrogen liquid container. The system is designed as a closed-loop to recycle helium. For tests conducted at cryogenic temperatures, specimens were exposed to either liquid helium or nitrogen pushed from a dewar using helium or nitrogen gas, respectively. The temperature measurement was conducted using a silicon diode located near the specimen that displays an accuracy of less than 1 Kelvin within a range of 1.4 to 500 Kelvin. The monotonic tensile tests were conducted at a quasi-static strain rate between 10^{-5} s^{-1} to 10^{-4} s^{-1} and were interrupted at multiple plastic strain values. The stress-displacement response along with the associated stress-strain curves are provided in Supplementary Fig. 2. The 0.2% offset yield strength values for all alloys as a function of temperature are reported in Table 1 and the specimen geometry along with the testing setup have been shown in Supplementary Fig. 1.

Fatigue testing

Very high cycle fatigue (VHCF) testing was performed on the medium-entropy CrCoNi alloy, the high-entropy CrMnFeCoNi alloy and the 316L stainless steel. For the CrCoNi and CrMnFeCoNi, the pure metals were vacuum induction melted and cast, after which the as-cast ingots were homogenized at 1200 °C for 48 h. Rotary swaging was used to reduce the diameter of the homogenized ingots from 40 mm to 10.7 mm. Cylindrical fatigue specimens with a gauge diameter of 3 mm and length of ~70 mm were machined from these rods and subjected to an annealing treatment at 1080 °C for 1 h for CrCoNi and at 1060 °C for 1 h for CrMnFeCoNi, followed by air cooling to obtain an average grain size of around 30 µm. The specimens were subjected to mechanical polishing and finished with a 3 µm diamond suspension prior to testing. A 3R™ VHCF MEG20TT ultrasonic fatigue testing frame was used to conduct the fatigue tests at room temperature. The specimens were designed to have their first tension-compression eigenmode at 20 kHz[86]. Potential self-heating was eliminated by employing the "pulse-pause" method[87], corresponding to 300 ms of cycling followed by 700 ms of rest. The tests were performed under fully reversed tension-compression loading, corresponding to a fatigue ratio of $R = -1$. The fatigue strength was determined at 5×10^8 cycles by adopting the staircase approach[88]. Low levels of alternating stress were initially applied after which power increments of 3% were made, corresponding to a stress increase of ~25 MPa. For any given stress level, if specimen failure did not occur after 5×10^8 cycles, the following test was conducted at an elevated stress level until failure. The general specimen geometry and the testing setup are shown in Supplementary Fig. 1.

Stacking fault energy calculation

Theoretical approach to stacking fault energy (SFE) calculation involves density functional theory (DFT) at 0 K and ab-initio molecular dynamics (AIMD) at finite temperatures via Vienna Ab-initio Simulation Package (VASP)[89]. First, the SFE calculation in DFT is performed following the atomic relaxation and determination of lattice constants for superlattice. We construct 270 atomic sites in the oriented lattice, aligning 9 {111} planes into z-direction. These 270 atomic sites are substituted by different constituent elements based on each alloy composition. The atomic configuration is established in special quasi-random structures via ATAT package[90], then fully relaxed and optimized for every lattice constant. We use volumetric-energy method in determination of lattice constant. Details of calculations in lattice constant are referred to the previous works[44,91]. After determining the lattice constants, we apply a slip at a different atomic plane, and calculate the SFEs. The SFE is calculated as below[92],

$$\gamma = \frac{E - E_0}{A} \tag{1}$$

where E_0 and E are energies of initial and deformed states, and A is an area of slip-plane. The DFT calculations are implemented within the projected-augmented-waves (PAW)[93] approach via Perdew-Burke-Ernzerhof (PBE)[94] exchange-correlation potentials. The PAW-PBE pseudopotentials for Ni, Co, Cr, Fe, Mn, and V are employed with the following valence electron configurations Ni ($3p^6\,3d^9\,4s^1$), Co ($3d^8\,4s^1$), Cr ($3p^6\,3d^5\,4s^1$), Fe ($3p^6\,3d^7\,4s^1$), Mn ($3p^6\,3d^6\,4s^1$), and V ($3s^2\,3p^6\,3d^4\,4s^1$), respectively. The oriented FCC superlattice with 270 atoms is employed with Monkhorst-pack k-mesh 2×2 for electronic minimization and ionic relaxation in allowing full distortions and lattice volumetric optimization, and $2 \times 2 \times 1$ for determining SFEs to hinder redundant SFs outside the periodic boundary. A 450 eV plane-wave energy cut-off is used for all the calculations. The tolerance criteria for energy and force are allowed within 1 meV and 5 meV/Å, respectively. For SFE of each alloy at finite temperatures, we employ ab-initio molecular dynamics (AIMD)[44,91]. This approach does not rely on 1) the empirical interatomic potential that is commonly used in the classical MD, and 2) the extrapolation of free energy from 0 K (such as quasi-harmonic approximation), so that we can more accurately estimate the SFEs at finite temperatures. For the electronic-minimization in AIMD, we use the same PAW-PBE pseudopotentials from the DFT calculation. A Nosé-Hoover thermostat is chosen for drawing an equilibrium state from a canonical ensemble of sampled states[95,96]. This introduces fictitious friction terms to permit temperature control into the Hamiltonian such that,

$$H' = \sum_{i=1}^{N} \frac{m_i}{2} s^2 (\dot{\vec{r}}_i)^2 - U_p(\vec{r}) + \frac{Q}{2} \dot{s}^2 + 3NkT\ln(s) \tag{2}$$

where N is the total number of atoms, m the mass of atom in i site, s the fictitious parameter introduced, $\vec{r}$ the position of atoms, so that the first two terms are kinetic and potential energy (U_p) of the given system. Q is the effective mass of s, k is the Boltzmann constant, and T is the temperature. We set $Q = 1$, and the simulation is controlled in 2 fs time-step (total 600 ~ 700 steps, *i.e.*, 1.2 ~ 1.4 ps), 450 eV plane-wave energy cut-off, and single k-point Γ mesh-grid. We use the optimized structures at 0 K as initial points. Among the multiple slip-cuts, we only select the one slip-cut that gives the maximum SFEs in each slip system, since it dictates the macroscopic deformation[44,91,97]. On the slip-cut of the maximum SFE, we set the temperatures of 77K and 300K for each

alloy. The equilibrated temperature along the time frame approaches the target temperature on average for all the calculations. The proper equilibrating step is determined by the minimum error of mean, ϵ. The error of mean at each cutoff step (i) is defined by $\epsilon_i = \sqrt{\frac{V_i}{N_{t,i}\kappa}}$, where V_i is variance, $N_{t,i}$ the number of data at each cutoff, and κ is correlation time based on autocorrelation such that,

$$\kappa = 1 + 2\sum_{j=1}^{N_t} \frac{1}{V(N_t - j)} \sum_{k=1}^{N_t - j} (X_k - \overline{X})(X_{k+j} - \overline{X}) \quad (3)$$

where V, $\overline{X}$, and N_t are variance, average, and total number of data for original X without cutoff. Total energies of undeformed or deformed structures have the converged value on average by excluding the data in non-equilibrating steps.

Data availability

The datasets generated during and/or analyzed during the current study are available from the corresponding author on request. Source data are provided with this paper.

Code availability

The code for center-of-symmetry calculation is not available online or publicly accessible, however it can be reproduced from references[79,99]. The dictionary indexing algorithm for EBSD data is described in reference[83]. The implementation for encoding Kikuchi/diffraction patterns can be readily reproduced following the procedure detailed in reference[85]. The associated train, test and validation datasets are publicly available[100].

References

1. Senkov, O. N., Miracle, D. B. & Firstov, S. A.*Metallic materials with high structural efficiency*, vol. 146 (Springer Science & Business Media, 2004).
2. Anoop, C. et al. A review on steels for cryogenic applications. *Mater. Perform. Charact.* **10**, 20200193 (2021).
3. Basuki, E. A., Prajitno, D. H. & Muhammad, F. Alloys developed for high temperature applications. In *AIP Conference Proceedings*, vol. 1805 (AIP Publishing, 2017).
4. Gludovatz, B. et al. A fracture-resistant high-entropy alloy for cryogenic applications. *Science* **345**, 1153–1158 (2014).
5. Ritchie, R. O. The conflicts between strength and toughness. *Nat. Mater.* **10**, 817–822 (2011).
6. Otto, F. et al. The influences of temperature and microstructure on the tensile properties of a cocrfemnni high-entropy alloy. *Acta Materialia* **61**, 5743–5755 (2013).
7. Ding, Q. et al. Real-time nanoscale observation of deformation mechanisms in crconi-based medium- to high-entropy alloys at cryogenic temperatures. *Mater. Today* **25**, 21–27 (2019).
8. Mishra, R. S., Haridas, R. S. & Agrawal, P. High entropy alloys - tunability of deformation mechanisms through integration of compositional and microstructural domains. *Mater. Sci. Eng.: A* **812**, 141085 (2021).
9. Stinville, J. et al. On the origins of fatigue strength in crystalline metallic materials. *Science* **377**, 1065–1071 (2022).
10. Mughrabi, H. Cyclic slip irreversibility and fatigue life: a microstructure-based analysis. *Acta Materialia* **61**, 1197–1203 (2013).
11. Mughrabi, H. Cyclic slip irreversibilities and the evolution of fatigue damage. *Metall. Mater. Trans. B* **40**, 431–453 (2009).
12. Mughrabi, H. Microstructural fatigue mechanisms: Cyclic slip irreversibility, crack initiation, non-linear elastic damage analysis. *Int. J. Fatigue* **57**, 2–8 (2013).
13. Forrest, P. G. et al. *Fatigue of Metals* (Elsevier, 2013).
14. Wang, P. et al. The highest fatigue strength for steels. *Acta Materialia* **289**, 120888 (2025).
15. Fleck, N., Kang, K. & Ashby, M. Overview no. 112: The cyclic properties of engineering materials. *Acta Metall. et. Materialia* **42**, 365–381 (1994).
16. Patel, S., deBarbadillo, J. & Coryell, S. Superalloy 718: Evolution of the alloy from high to low temperature application. In Ott, E. et al. (eds.) *Proceedings of the 9th International Symposium on Superalloy 718 & Derivatives: Energy, Aerospace, and Industrial Applications*, 23–49 (Springer International Publishing, Cham, 2018).
17. Gell, M., Leverant, G. & Wells, C. The fatigue strength of nickel-base superalloys. *ASTM STP* **467**, 113–153 (1970).
18. Kang, L. & Yang, C. A review on high strength titanium alloys: Microstructure, strengthening, and properties. *Adv. Eng. Mater.* **21**, 1801359 (2019).
19. Stinville, J. et al. Direct measurements of slip irreversibility in a nickel-based superalloy using high resolution digital image correlation. *Acta Materialia* **186**, 172–189 (2020).
20. Polák, J. & Man, J. Initiation of stage I fatigue cracks - experiments and models. *Procedia Eng.* **101**, 386–394 (2015).
21. Ferro, A., Mazzetti, P. & Montalenti, G. On the effect of the crystalline structure on fatigue: Comparison between body-centred metals (ta, nb, mo and w) and face-centred and hexagonal metals. *Philos. Mag.: A J. Theor. Exp. Appl. Phys.* **12**, 867–875 (1965).
22. Buck, A. Fatigue properties of pure metals. *Int. J. Fract. Mech.* **3**, 145–152 (1967).
23. Wu, H. & Fan, G. An overview of tailoring strain delocalization for strength-ductility synergy. *Prog. Mater. Sci.* **113**, 100675 (2020).
24. Ahmadikia, B., Beyerlein, A. L., Hestroffer, J. M., Kumar, M. A. & Beyerlein, I. J. Designing ti-6al-4v microstructure for strain delocalization using neural networks. *J. Mater. Sci.: Mater. Theory* https://doi.org/10.1186/s41313-024-00055-9 (2024).
25. Anjaria, D. et al. Plastic deformation delocalization at cryogenic temperatures in a nickel-based superalloy. *Acta Materialia* **276**, 120106 (2024).
26. Stinville, J. et al. Measurement of elastic and rotation fields during irreversible deformation using heaviside-digital image correlation. *Mater. Charact.* **169**, 110600 (2020).
27. Bourdin, F. et al. Measurements of plastic localization by heaviside-digital image correlation. *Acta Materialia* **157**, 307–325 (2018).
28. Yang, B. et al. Grain size dependence of microscopic strain distribution in a high entropy alloy at the onset of plastic deformation. *Acta Materialia* **285**, 120682 (2025).
29. Jullien, M., Black, R., Stinville, J., Legros, M. & Texier, D. Grain size effect on strain localization, slip-grain boundary interaction and damage in the alloy 718 ni-based superalloy at 650 °c. *Mater. Sci. Eng.: A* **912**, 146927 (2024).
30. Mello, A. W., Nicolas, A., Lebensohn, R. A. & Sangid, M. D. Effect of microstructure on strain localization in a 7050 aluminum alloy: Comparison of experiments and modeling for various textures. *Mater. Sci. Eng.: A* **661**, 187–197 (2016).
31. Alaie, A. et al. Effect of microstructure pattern on the strain localization in dp600 steels analyzed using combined in-situ experimental test and numerical simulation. *Mater. Sci. Eng.: A* **638**, 251–261 (2015).
32. Loretto, M., Phillips, P. & Mills, M. Stacking fault tetrahedra in metals. *Scr. Materialia* **94**, 1–4 (2015).
33. Kiritani, M. Story of stacking fault tetrahedra. *Mater. Chem. Phys.* **50**, 133–138 (1997).
34. Zhang, L., Lu, C., Michal, G., Deng, G. & Tieu, K. The formation and destruction of stacking fault tetrahedron in fcc metals: A molecular dynamics study. *Scr. Materialia* **136**, 78–82 (2017).
35. Savage, J. C. Dislocation pileup as a representation of strain accumulation on a strike-slip fault. *J. Geophys. Res.: Solid Earth*

https://doi.org/10.1029/2005JB004021, https://agupubs.onlinelibrary.wiley.com/doi/pdf/10.1029/2005JB004021 (2006).
36. Chakravarthy, S. S. & Curtin, W. Effect of source and obstacle strengths on yield stress: A discrete dislocation study. *J. Mech. Phys. Solids* **58**, 625–635 (2010).
37. Heczko, M. et al. Role of deformation twinning in fatigue of CrCoNi medium-entropy alloy at room temperature. *Scr. Materialia* **202**, 113985 (2021).
38. Pandey, P. et al. On the faulting and twinning mediated strengthening and plasticity in a gamma strengthened coni-based superalloy at room temperature. *Acta Materialia* **252**, 118928 (2023).
39. Yang, C. et al. Chemical inhomogeneity-induced profuse nanotwinning and phase transformation in AuCu nanowires. *Nat. Commun.* **14**, 5705 (2023).
40. Ma, E. & Liu, C. Chemical inhomogeneities in high-entropy alloys help mitigate the strength-ductility trade-off. *Prog. Mater. Sci.* **143**, 101252 (2024).
41. Wei, D. et al. Metalloid substitution elevates simultaneously the strength and ductility of face-centered-cubic high-entropy alloys. *Acta Materialia* **225**, 117571 (2022).
42. Zhang, Q. et al. Room-temperature super-elongation in high-entropy alloy nanopillars. *Nat. Commun.* **14**, 7469 (2023).
43. You, D., Celebi, O. K., Mohammed, A. S. K. & Sehitoglu, H. Negative stacking fault energy in fcc materials-its implications. *Int. J. Plasticity* **170**, 103770 (2023).
44. You, D. et al. Short-range ordering mechanics in fcc materials. *Int. J. Plasticity* **174**, 103919 (2024).
45. Yang, D. C., Jo, Y. H., Ikeda, Y., Körmann, F. & Sohn, S. S. Effects of cryogenic temperature on tensile and impact properties in a medium-entropy vconi alloy. *J. Mater. Sci. Technol.* **90**, 159–167 (2021).
46. Fang, Y. et al. An in situ ambient and cryogenic transmission electron microscopy study of the effects of temperature on dislocation behavior in CrCoNi-based high-entropy alloys with low stacking-fault energy. *Appl. Phys. Lett.* https://doi.org/10.1063/5.0069086 (2021).
47. Ma, D., Grabowski, B., Körmann, F., Neugebauer, J. & Raabe, D. Ab initio thermodynamics of the cocrfemnni high entropy alloy: Importance of entropy contributions beyond the configurational one. *Acta Materialia* **100**, 90–97 (2015).
48. Zhao, S., Stocks, G. M. & Zhang, Y. Stacking fault energies of face-centered cubic concentrated solid solution alloys. *Acta Materialia* **134**, 334–345 (2017).
49. Oliveros, D. et al. Orientation-related twinning and dislocation glide in a cantor high entropy alloy at room and cryogenic temperature studied by in situ tem straining. *Mater. Chem. Phys.* **272**, 124955 (2021).
50. Gu, P., Dao, M. & Suresh, S. Analysis of size-dependent slip transfer and inter-twin flow stress in a nanotwinned fcc metal. *Acta Materialia* **67**, 409–417 (2014).
51. Wu, Z., Zhang, Y. & Srolovitz, D. Dislocation-twin interaction mechanisms for ultrahigh strength and ductility in nanotwinned metals. *Acta Materialia* **57**, 4508–4518 (2009).
52. Xie, B. et al. Divergent evolution of slip banding in CrCoNi alloys. *Nat. Commun.* https://doi.org/10.1038/s41467-025-58480-4 (2025).
53. Frank, F. C. & Read, W. T. Multiplication processes for slow moving dislocations. *Phys. Rev.* **79**, 722–723 (1950).
54. Chen, X. et al. Direct observation of chemical short-range order in a medium-entropy alloy. *Nature* **592**, 712–716 (2021).
55. Hsiao, H.-W. et al. Data-driven electron-diffraction approach reveals local short-range ordering in CrCoNi with ordering effects. *Nat. Commun.* **13**, 6651 (2022).
56. Wolf, K., Gudladt, H.-J., Calderon, H. & Kostorz, G. Transition between planar and wavy slip in cyclically deformed short-range ordered alloys. *Acta Metall. et. Materialia* **42**, 3759–3765 (1994).
57. Ma, E. Unusual dislocation behavior in high-entropy alloys. *Scr. Materialia* **181**, 127–133 (2020).
58. Ma, S. et al. Chemical short-range ordering regulated dislocation cross slip in high-entropy alloys. *J. Alloy. Compd.* **911**, 165144 (2022).
59. Abu-Odeh, A. & Asta, M. Modeling the effect of short-range order on cross-slip in an fcc solid solution. *Acta Materialia* **226**, 117615 (2022).
60. Han, D., Wang, Z., Yan, Y., Shi, F. & Li, X. A good strength-ductility match in cu-mn alloys with high stacking fault energies: Determinant effect of short range ordering. *Scr. Materialia* **133**, 59–64 (2017).
61. Zhang, Y., Han, D. & Li, X. A unique two-stage strength-ductility match in low solid-solution hardening ni-cr alloys: Decisive role of short range ordering. *Scr. Materialia* **178**, 269–273 (2020).
62. Cenedese, P., Bley, F. & Lefebvre, S. Atomic short range order in a fe-ni invar alloy. *MRS Proc.* **21**, 351 (1982).
63. Li, L. et al. Evolution of short-range order and its effects on the plastic deformation behavior of single crystals of the equiatomic CrCoNi medium-entropy alloy. *Acta Materialia* **243**, 118537 (2023).
64. Yu, Y. et al. Temperature-dependent short-range order formation and its effects on yield strength in single crystals of the equiatomic Cr-Mn-Fe-Co-Ni high-entropy alloy. *J. Alloy. Compd.* **1014**, 178559 (2025).
65. Lu, K. et al. Superior low-cycle fatigue properties of cocrni compared to cocrfemnni. *Scr. Materialia* **194**, 113667 (2021).
66. Ghomsheh, M. Z. et al. High cycle fatigue deformation mechanisms of a single phase crmnfeconi high entropy alloy. *Mater. Sci. Eng.: A* **777**, 139034 (2020).
67. Li, P., Li, S., Wang, Z. & Zhang, Z. Fundamental factors on formation mechanism of dislocation arrangements in cyclically deformed fcc single crystals. *Prog. Mater. Sci.* **56**, 328–377 (2011).
68. Pham, M., Holdsworth, S., Janssens, K. & Mazza, E. Cyclic deformation response of aisi 316l at room temperature: Mechanical behaviour, microstructural evolution, physically-based evolutionary constitutive modelling. *Int. J. Plasticity* **47**, 143–164 (2013).
69. Chen, Q. et al. Small crack behavior and fracture of nickel-based superalloy under ultrasonic fatigue. *Int. J. Fatigue* **27**, 1227–1232 (2005).
70. Kolyshkin, A., Zimmermann, M., Kaufmann, E. & Christ, H.-J. Experimental investigation and analytical description of the damage evolution in a ni-based superalloy beyond 106 loading cycles. *Int. J. Fatigue* **93**, 272–280 (2016).
71. Stöcker, C., Zimmermann, M. & Christ, H.-J. Effect of precipitation condition, prestrain and temperature on the fatigue behaviour of wrought nickel-based superalloys in the vhcf range. *Acta Materialia* **59**, 5288–5304 (2011).
72. Stöcker, C., Zimmermann, M. & Christ, H.-J. Localized cyclic deformation and corresponding dislocation arrangements of polycrystalline ni-base superalloys and pure nickel in the vhcf regime. *Int. J. Fatigue* **33**, 2–9 (2011).
73. Marti, N., Favier, V., Gregori, F. & Saintier, N. Correlation of the low and high frequency fatigue responses of pure polycrystalline copper with mechanisms of slip band formation. *Mater. Sci. Eng.: A* **772**, 138619 (2020).
74. Chen, F., Liu, F., Tan, Y.-B., Shi, W. & Xiang, S. Breaking the strength-ductility trade-off via heterogeneous structure in fecocrnimo0.2 high-entropy alloy. *J. Mater. Res. Technol.* **29**, 265–275 (2024).

75. An, Z. et al. Hierarchical grain size and nanotwin gradient microstructure for improved mechanical properties of a non-equiatomic cocrfemnni high-entropy alloy. *J. Mater. Sci. Technol.* **92**, 195–207 (2021).
76. Kang, J. & Cem Tasan, C. Beyond the dynamic hall-petch effect: Mechanical twinning for microscopic strain delocalization. *Scr. Materialia* **255**, 116346 (2025).
77. Charpagne, M. et al. Automated and quantitative analysis of plastic strain localization via multi-modal data recombination. *Mater. Charact.* **163**, 110245 (2020).
78. Phillips, P., Brandes, M., Mills, M. & De Graef, M. Diffraction contrast stem of dislocations: Imaging and simulations. *Ultramicroscopy* **111**, 1483–1487 (2011).
79. Vorontsov, V., Kovarik, L., Mills, M. & Rae, C. High-resolution electron microscopy of dislocation ribbons in a CMSX-4 superalloy single crystal. *Acta Materialia* **60**, 4866–4878 (2012).
80. Niu, C., LaRosa, C. R., Miao, J., Mills, M. J. & Ghazisaeidi, M. Magnetically-driven phase transformation strengthening in high entropy alloys. *Nat. Commun.* **9**, 1363 (2018).
81. Montgomery, C. B., Koohbor, B. & Sottos, N. R. A robust patterning technique for electron microscopy-based digital image correlation at sub-micron resolutions. *Exp. Mech.* **59**, 1063–1073 (2019).
82. Valle, V. et al. Crack analysis in mudbricks under compression using specific development of stereo-digital image correlation. *Exp. Mech.* https://doi.org/10.1007/s11340-017-0363-2 (2017).
83. Lenthe, W., Germain, L., Chini, M., Gey, N. & De Graef, M. Spherical indexing of overlap ebsd patterns for orientation-related phases - application to titanium. *Acta Materialia* **188**, 579–590 (2020).
84. Sharma, J., Nicolaÿ, A., De Graef, M. & Bozzolo, N. Phase discrimination between gamma and eta phases in the new nickel-based superalloy Vdm Alloy 780 using ebsd. *Mater. Charact.* **176**, 111105 (2021).
85. Calvat, M. et al. Learning metal microstructural heterogeneity through spatial mapping of diffraction latent space features. *npj Comput. Mater.* https://doi.org/10.1038/s41524-025-01770-8 (2025).
86. Stanzl-Tschegg, S. Very high cycle fatigue measuring techniques. *Int. J. Fatigue* **60**, 2–17 (2014).
87. Stanzl, S. A new experimental method for measuring life time and crack growth of materials under multi-stage and random loadings. *Ultrasonics* **19**, 269–272 (1981).
88. Stäcker, C. & Sander, M. Experimental, analytical and numerical analyses of constant and variable amplitude loadings in the very high cycle fatigue regime. *Theor. Appl. Fract. Mech.* **92**, 394–409 (2017).
89. Kresse, G. & Furthmüller, J. Efficient iterative schemes for ab initio total-energy calculations using a plane-wave basis set. *Phys. Rev. B* **54**, 11169–11186 (1996).
90. van de Walle, A. et al. Efficient stochastic generation of special quasirandom structures. *Calphad* **42**, 13–18 (2013).
91. You, D., Celebi, O. K., Mohammed, A. S. K., Bucsek, A. & Sehitoglu, H. The derivation of crss in pure ti and ti-al alloys. *Int. J. Plasticity* **184**, 104187 (2025).
92. Vítek, V. Intrinsic stacking faults in body-centred cubic crystals. *Philos. Mag.: A J. Theor. Exp. Appl. Phys.* **18**, 773–786 (1968).
93. Kresse, G. & Joubert, D. From ultrasoft pseudopotentials to the projector augmented-wave method. *Phys. Rev. B* **59**, 1758–1775 (1999).
94. Perdew, J. P., Burke, K. & Ernzerhof, M. Generalized gradient approximation made simple. *Phys. Rev. Lett.* **77**, 3865–3868 (1996).
95. Hoover, W. G. Canonical dynamics: equilibrium phase-space distributions. *Phys. Rev. A* **31**, 1695–1697 (1985).
96. Nosé, S. A unified formulation of the constant temperature molecular dynamics methods. *J. Chem. Phys.* **81**, 511–519 (1984).
97. You, D. et al. Inverse design of short-range order arrangement via neural network. *Int. J. Solids Struct.* **309**, 113175 (2025).
98. Wong, B. Points of view: Color blindness. *Nat Methods* **8**, 441 (2011).
99. Li, J. Central symmetry parameter http://li.mit.edu/Archive/Graphics/A/Doc/CentralSymmetry.pdf (2003).
100. Calvat, M., Anjaria, D., Wang, H., Vecchio, K. & Stinville, J.-C. Kikuchi pattern dataset from wrought and as-built additively manufactured superalloys, https://doi.org/10.5061/DRYAD.ZCRJDFNR9 (2025).

Acknowledgements

This is a colorblind-friendly version (protanopia) following the guidance from Colour Blind Awareness[98]. The color-blind version of this article has been made possible thanks to funding from the NSF (award #2338346). J.C.S., D.A., M.C. and S.S. acknowledge the National Science Foundation (NSF) DMR CAREER Award #2338346 for research funding. H.S. and D.Y. acknowledge the National Science Foundation (NSF) CMMI Award #21-25821 for research funding. This work was carried out in the Materials Research Laboratory Central Research Facilities, University of Illinois. M.H. acknowledges financial support from the Czech Science Foundation under the Junior Star project with contract No. 24-11058M. The use of CEITEC Nano Research Infrastructure, supported by the CzechNanoLab project LM2023051 funded by MEYS CR, is gratefully acknowledged. A.S.T. acknowledges support from the DFG through project No. 553555345 (SR 170/2-1).

Author contributions

D.A: Conceptualization, Data curation, Formal analysis, Investigation, Methodology, Resources, Writing—original draft, Writing - review & editing. M.H.: Investigation, Methodology, Verification, Writing - review & editing. D.Y: Formal analysis, Resources, Writing—original draft, Writing - review & editing. M.C.: Verification, Resources, Writing—review & editing. S.S.: Investigation, Verification, Writing—review & editing. M.R.: Resources. A.S.T: Resources. H.S.: Resources, Verification, Writing—review & editing. G.L: Resources, Writing—original draft, Writing—review & editing. J.C.S.: Conceptualization, Funding acquisition, Methodology, Project administration, Resources, Supervision, Writing—original draft, Writing - review & editing.

Competing interests

The authors declare no competing interests.

Additional information

Supplementary information The online version contains supplementary material available at https://doi.org/10.1038/s41467-026-69046-3.

Correspondence and requests for materials should be addressed to Dhruv Anjaria or J. C. Stinville.

Peer review information *Nature Communications* thanks Christopher Hutchinson and the other, anonymous, reviewer(s) for their contribution to the peer review of this work. A peer review file is available.